



Doping effect of phosphate in Bi_2WO_6 and universal improved photocatalytic activity for removing various pollutants in water

Chunmei Li^a, Gang Chen^{a,*}, Jingxue Sun^{a,*}, Jiancun Rao^b, Zhonghui Han^a, Yidong Hu^a, Weinan Xing^a, Congmin Zhang^a

^a Department of Chemistry, Harbin Institute of Technology, Harbin 150001, PR China

^b School of Materials Science and Engineering, Harbin Institute of Technology, 150001, PR China

ARTICLE INFO

Article history:

Received 3 November 2015

Received in revised form 19 January 2016

Accepted 23 January 2016

Available online 31 January 2016

Keywords:

Bi_2WO_6 photocatalyst

Anionic group doping

Various pollutant removal

Band structure regulation

Effective charge separation

ABSTRACT

Ionic group doping into the semiconductor photocatalyst is a new concept to improve photocatalytic performance, which always is a difficult challenge. In this paper, PO_4 -doped Bi_2WO_6 photocatalyst is prepared by the urea-precipitation way in the hydrothermal process for the first time. The as-prepared sample presents the universal enhanced photocatalytic activity for removing various contaminants in water compared with the pristine Bi_2WO_6 under visible-light irradiation, such as heavy metal Cr (VI), colored dye RhB, colorless phenol and different kind antibiotics. It attributes to the doping effect of PO_4 group in Bi_2WO_6 influencing on energy band structure, light absorption property and separation efficiency of the charge carriers. This work provides a new insight into anionic group doping effects and takes an important step toward the development of improving Bi-based photocatalyst activity.

© 2016 Elsevier B.V. All rights reserved.

1. Introduction

Water pollution has become one of the most serious environmental problems over the past few decades, which constantly threatens the human health and sustainable development of society. In order to solve the increasing water pollution crisis, the semiconductor photocatalytic technique has drawn wide attention and become a hot research topic as one of the most simple, economic and effective ways to decompose pollutants with high toxicity from wastewater [1–3]. Among the varied semiconductor photocatalyst, TiO_2 has always been considered as a quite promising photocatalyst for wastewater treatment due to its superior photocatalytic activity, photochemical stability and nontoxicity [4–6]. However, an inevitable disadvantage of TiO_2 is that it can be only excited by the ultraviolet light due to its wide band gap, thus limiting its practical applications to a large extent [7,8]. For utilizing solar energy efficiently, a lot of visible-light-driven photocatalysts have been developed in recent years.

Among the reported visible-light photocatalysts, Bi_2WO_6 has caused the extensive attention because of its unique layered structure feature, superior band composition and relatively high photostability [9–11]. It is believed that Bi_2WO_6 can be acted as a potential promising photocatalyst for degrading organic pol-

lutants in water system. However, improving the photocatalytic performance of Bi_2WO_6 to satisfy the practical application for environmental cleaning is still a big challenge because of its short photogenerated charge carrier lifetime which is a main impact factor for the photocatalytic activity [12,13]. To overcome the above drawback and further improve photocatalytic activity of Bi_2WO_6 under visible light irradiation, doping with suitable impurity is a good choice [14,15]. It involves the intentional incorporation of suitable cations or anions into the host lattices and changes semiconductor electrical properties by increasing electron or hole densities, which can adjust the composition of semiconductor photocatalysts effectively to facilitate the separation of photoinduced electron-hole pairs [16,17]. To date, doping suitable ions into Bi_2WO_6 crystal lattice for improving its photocatalytic activity have been reported by many groups. For example, Wang's group has reported the Er^{3+} doped Bi_2WO_6 photocatalysts, which could transform visible light beyond the absorption edge of Bi_2WO_6 into ultraviolet light to activate Bi_2WO_6 [18]. Zhu et al. has also reported that the F-substituted Bi_2WO_6 ($\text{Bi}_2\text{WO}_{6-x}\text{F}_x$) photocatalysts prepared by a reflux and subsequent calcination method, which enhanced the mobility rate of photoexcited charge carriers and made the valence band position possess a stronger oxidation power [19]. Zhang's group obtained bismuth self-doping of Bi_2WO_6 that realized the efficient sodium pentachlorophenate removal under visible light [20]. All the doping modes above enhanced the photocatalytic activity of Bi_2WO_6 obviously under visible light irradiation. However, compared with the simple ion doping, ionic

* Corresponding authors. Fax: +86 451 86413753.

E-mail addresses: gchen@hit.edu.cn (G. Chen), jxsun@hit.edu.cn (J. Sun).

group constituted by various atoms acting as dopant may provide more possibilities for adjusting the crystal structure, optimizing light absorption properties and thus improving photocatalytic activities of the semiconductors. For instance, Lee et al. reported the oxyanion PO_4 doping into the BiVO_4 photocatalyst, which had a great impact on the photoelectrochemical or photocatalytic activity of m-BiVO_4 under visible light illumination [21]. Huang and et al. reported CO_3^{2-} anionic group self-doped into $\text{Bi}_2\text{O}_2\text{CO}_3$, which extended the photoresponse range of $\text{Bi}_2\text{O}_2\text{CO}_3$ from UV to visible light and enhanced the visible light absorption by tuning its band gap continuously [22]. Those superior results endow us to design a novel ionic group doped into Bi_2WO_6 photocatalyst to improve its photocatalytic activity dramatically and extend its applied range for meeting the practical requirement.

Herein, in this work, the anionic group PO_4 is introduced into Bi_2WO_6 via the urea-precipitation strategy for the first time, which replaces some of WO_4 in Bi_2WO_6 . In comparison with the pristine Bi_2WO_6 , the PO_4 doped Bi_2WO_6 exhibits superior photocatalytic degradation activity for various contaminants in the water under visible light, including heavy metal Cr (VI), colored dye RhB, colorless phenol and different kind antibiotics. The origin of the enhanced photocatalytic activity of PO_4 doped Bi_2WO_6 is mainly attributed to the effective separation of photogenerated electron-hole pairs, which is elucidated by employing photoluminescent spectrum, fluorescence decay, photoelectrochemical properties et al. characterizations. This work extends the development of Bi_2WO_6 photocatalyst and launches an exemplificative strategy for doping ionic group in other Bi-based oxides to improve photocatalytic activity.

2. Experimental section

2.1. Preparation and characterizations

All materials were purchased from commercial sources and used without further purification. Samples of PO_4 -doped Bi_2WO_6 were prepared via the urea-precipitation method [23]. In a typical procedure, firstly, sodium tungstate ($\text{Na}_2\text{WO}_4 \cdot 2\text{H}_2\text{O}$) and sodium phosphate (Na_3PO_4) mixed solution was added into the bismuth nitrate ($\text{Bi}(\text{NO}_3)_3 \cdot 5\text{H}_2\text{O}$) solution drop by drop in a stoichiometric ratio under vigorous magnetic stirring for 1 h, then this suspension added 0.5g of urea was transferred into a 25 ml Teflon lined stainless steel autoclave to carry out hydrothermal process 24 h at 160°C . After cooling down to room temperature, the solid sample was collected by centrifugation and washed with deionized water and ethanol in turn.

The phase of as-prepared Bi_2WO_6 sample was characterized by powder X-ray diffractometer (XRD, RigakuD/max-2000) equipped with a $\text{Cu-K}\alpha$ radiation at a scanning rate of 5°min^{-1} in the 2θ range of $10\text{--}90^\circ$. X-ray tube voltage and current were set at 45 kV and 50 mA, respectively. The morphologies of samples were characterized by field-emission scanning electron microscopy (FESEM, FEI QUANTA 200F). Transmission electron microscopy (TEM) and high-resolution TEM (HR-TEM) of samples were also carried out on FEI Tecnai G2 S-Twin and they are operated at 300 kV. X-ray photoelectron spectroscopy (XPS) analysis was measured on an American electronics physical system (HI5700ESCA) with X-ray photoelectron spectroscope using $\text{Al K}\alpha$ (1486.6 eV) monochromatic X-ray radiation. The peak positions were corrected against the contaminated carbon C 1s peak (284.6 eV). The UV–vis diffuse reflectance spectra (DRS) of the samples were recorded on a UV–vis spectrophotometer (PG, UH-4150) with BaSO_4 as the background between 250 nm and 900 nm at room temperature. The nitrogen adsorption and desorption isotherm, pore size distribution and specific surface area were measured using an AUTOSORB-1 surface area and pore size analyzer at 77 K. The photoluminescent and fluores-

cence decay spectra were measured by the FLUOROMAX-4C-TCSPC at room temperature. The electron paramagnetic resonance (EPR) was carried out on the BRUKER (ER083cs) at the room temperature to detect oxygen vacancy. Energy dispersive X-ray fluorescence (EDXRF) was executed on the AXIOS-PW4400 at the room temperature. The electron spin resonance (ESR) analysis was conducted with a Bruker EPR A 300-10/12 spectrometer to detect radicals.

2.2. Photocatalytic and photoelectrochemical measurements

The photocatalytic activities were evaluated by Cr (IV) solution, RhB dye, phenol solution and various antibiotics degradation under visible light irradiation. A 300 W Xe lamp with a filter ($\lambda > 400 \text{ nm}$) was served as visible light source. The photodegradation of Cr (IV), RhB dye and phenol solution were performed at room temperature as follows: after the Cr (IV), RhB dye and phenol solutions (100 ml, 10 mg L^{-1}) containing 0.05 g Bi_2WO_6 was carried out about 5 min ultrasonic process, respectively, it was magnetic stirring 55 min in dark to achieve adsorption-desorption equilibrium between photocatalysts and pollutants. Then 0.05 g citric acid was added in the Cr (IV) solution and 0.1 ml H_2O_2 was added in the phenol solution before irradiation. Every 10 min of time intervals, 3 ml mixture was collected from the suspension liquid, followed by centrifuged at 10^4 rpm for 3 min. The absorbance of Cr (IV) solution determined using the diphenylcarbazide method and RhB (phenol) solution was analyzed by measuring the absorbance at $\lambda = 554 \text{ nm}$ (270 nm) through UV–vis spectrophotometer (PG, TU-1901). The method of photocatalytic decomposition antibiotics including gatifloxacin (GFLX), Danofloxacin mesylate (DFLXM), Ciprofloxacin (CPFX) and Enrofloxacin hydrochloride (ENRO) are as follows: 0.1 g photocatalyst was suspended in an aqueous solution of antibiotics (100 ml, 20 mg L^{-1}). In order to reach adsorption/desorption equilibration, the suspension was magnetic stirring constantly in dark for 1 h. During the photocatalytic reaction process, air was blown into the reaction medium. At irradiation time interval of every 15 min, 3 ml solution was sampled and magnetic separated, then monitoring the absorbance of antibiotics at $\lambda = 285 \text{ nm}$ (GFLX), 278 nm (DFLXM), 274 nm (ENRO) and 278 nm (CPFX), respectively.

Meanwhile, the radicals capture experiments is analogous to the photocatalytic degradation experiments. They were carried out by adding 1 mmol triethanolamine (TEOA, a quencher of h^+), 1 mmol Dimethyl sulfoxide (DMSO, a quencher of $\bullet\text{OH}$), 1 mmol isopropanol (IPA, a quencher of $\bullet\text{OH}$) and 1 mmol benzoquinone (BQ, a quencher of $\bullet\text{O}_2^-$), respectively. The concentration of RhB and CPFX in solution was determined through UV–vis spectrophotometer. The photodegradation efficiency was calculated according to $\eta = (C_0 - C)/C_0$.

where η is the photodegradation efficiency; C_0 is the initial concentration of reactant before illumination; C is the reactant concentration after illumination time.

The photoelectrochemical properties were measured in the AUT 86258 electrochemical working station employing a standard three-compartment cell under visible light assembled by a 300 W Xe lamp with a filter ($\lambda > 400 \text{ nm}$). The samples coated at FTO glass, a kind of Ag/AgCl electrode, a piece of Pt sheet, and 0.01 M sodium carbonate were used as the working electrode, reference electrode, counter-electrode and electrolyte, respectively.

3. Results and discussion

3.1. Structure and composition of the as-prepared Bi_2WO_6 photocatalysts

The XRD patterns of pristine Bi_2WO_6 (BWO) and PO_4 -doped Bi_2WO_6 samples with different doping ratios (the sample with doping ratio of 1%, 3%, 5% and 10% are represented by BWO-P1, BWO-P3, BWO-P5 and BWO-P10, respectively) are shown in Fig. 1a.

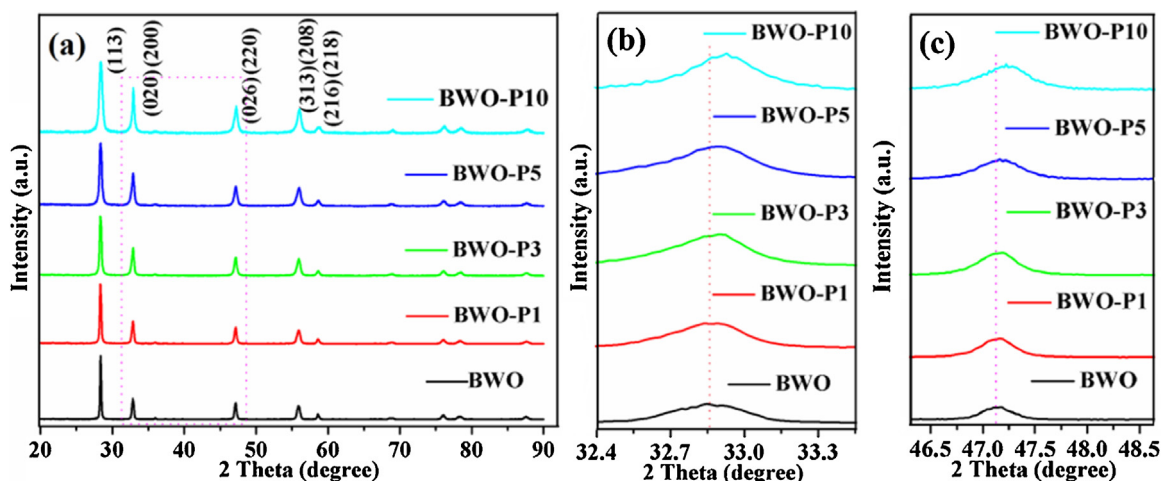


Fig. 1. XRD patterns of BWO, BWO-P1, BWO-P3, BWO-P5 and BWO-P10 (a), magnified peaks at (020) and (220) (b-c).

Table 1
EDXRF results of PO₄-doped Bi₂WO₆ samples.

Sample	Element	Wt%	Atomic%	Composition
BWO-P1	P	0.037	0.0012	(BiO) ₂
	W	23.997	0.132	(WO ₄) _{0.992} (PO ₄) _{0.008}
BWO-P3	P	0.098	0.0032	(BiO) ₂
	W	22.936	0.125	(WO ₄) _{0.98} (PO ₄) _{0.02}
BWO-P5	P	0.246	0.0059	(BiO) ₂
	W	21.749	0.118	(WO ₄) _{0.96} (PO ₄) _{0.04}
BWO-P10	P	0.321	0.01	(BiO) ₂
	W	18.973	0.103	(WO ₄) _{0.91} (PO ₄) _{0.09}

These five patterns are identical to the standard spectrum of pure orthorhombic Bi₂WO₆ (JCPDS card No. 73-1126), indicating that doped PO₄ does not change the crystalline phase of Bi₂WO₆. With increasing PO₄ doping amount, the magnified view of three peaks at (113) (Fig. S1), (020) (Fig. 1b) and (220) (Fig. 1c) shows regularly shift toward higher angles compared to that of pure Bi₂WO₆. According to Bragg's law ($n\lambda = 2d\sin\theta$), a bigger 2θ value indicates a smaller lattice spacing [24]. So such the slight shift of peaks is expected because P has a smaller ionic radius and higher electronegativity compared to W, thus making lattice spacing smaller. These XRD results indicate that PO₄ has been well inserted into the Bi₂WO₆ lattice and replaces the WO₄ site to realize uniform doping. In addition, the real atomic ratios between tungsten and phosphorus of the different PO₄-doped Bi₂WO₆ samples are further determined by the EDXRF analysis. Table 1 presents that the actual atomic doping ratios of phosphorus in the PO₄-doped Bi₂WO₆ samples are also the same as those introduced initially during the synthesis. The slight reduction may be due to a handful of PO₄ having not doped into the Bi₂WO₆ lattice but dissolved in water and removed during the purification step [21].

It is known that Raman scattering is an effective method to investigate the lattice strain of nanomaterial semiconductor [25,26]. Fig. 2a shows Raman spectra of PO₄-doped Bi₂WO₆ samples with different doping ratios. Those samples exhibit major bands located at in the range of 200–450 cm⁻¹ and 600–1000 cm⁻¹, respectively, which is almost unanimous with the results reported in the literature [27,28]. The peaks in the range of 600–1000 cm⁻¹ can be assigned to the stretches of the W–O bands [29] and the peak at 303 cm⁻¹ can be ascribed to the translation modes involving simultaneous motions of Bi and WO₄, respectively [30]. In detail, compared with those of pure Bi₂WO₆, the peaks located at about 280 cm⁻¹ and 303 cm⁻¹ shift to higher vibrational frequencies and no obvious shift is observed at 600–1000 cm⁻¹ with the increase of the doping ratio of PO₄ (Fig. 2b), which originates from the incorpo-

ration of substitutional PO₄ dopant effect as expected. Furthermore, after the hexavalent lattice W is replaced by pentavalent P, the P–O bond is existed in the lattice. The length of the W–O bond is longer than that of the P–O bond in the lattice because P has a smaller ionic radius and higher electronegativity compared to W. As a result, a tensile stress in the lattice is induced, leading to the increase of vibrational energy of the 303 cm⁻¹ peak which corresponds to the simultaneous motions of Bi and WO₄. Therefore, the peaks at 303 cm⁻¹ for PO₄-doped Bi₂WO₆ samples shift to higher frequencies compared with the pure Bi₂WO₆. Meanwhile, the tensile stress of the W–O bond in the lattice cannot change, thus no peaks shift in the range of 600–1000 cm⁻¹ are observed. These Raman scattering results also confirms that PO₄ is successfully introduced into the Bi₂WO₆ lattice and replaces the WO₄ site.

3.2. Morphology characteristic of as-prepared photocatalysts

The sample micromorphology feature is investigated by FESEM. PO₄ doping ratio has large influence on the Bi₂WO₆ morphology. The pristine Bi₂WO₆ sample exhibits nanoplates morphology features (Fig. S2a), as a contrast, the morphology of PO₄-doped Bi₂WO₆ samples gradually converts from 2D nanoplates to 3D microspherical architectures with increasing the PO₄ doping ratio (Fig. S2). The BWO-P5 and BWO-P10 samples show uniform microsphere structure built by self-assembly of 2D nanosheets with a diameter of 8–10 μm (Fig. S2d and S2e). The aggregation of the unit nanosheets can result in generating numerous hierarchical pores on nanoscale, which may enhance the physicochemical properties and act as transport paths for small molecules [31]. The BET specific surface areas of the samples are measured to be 5.6, 10.6, 13.8, 16.7 and 19.8 cm² g⁻¹ for the BWO, BWO-P1, BWO-P3, BWO-P5 and BWO-P10 samples, respectively. Obviously, the surface area gradually increases with increasing PO₄ ratio, which is in favor of improving photocatalytic activity.

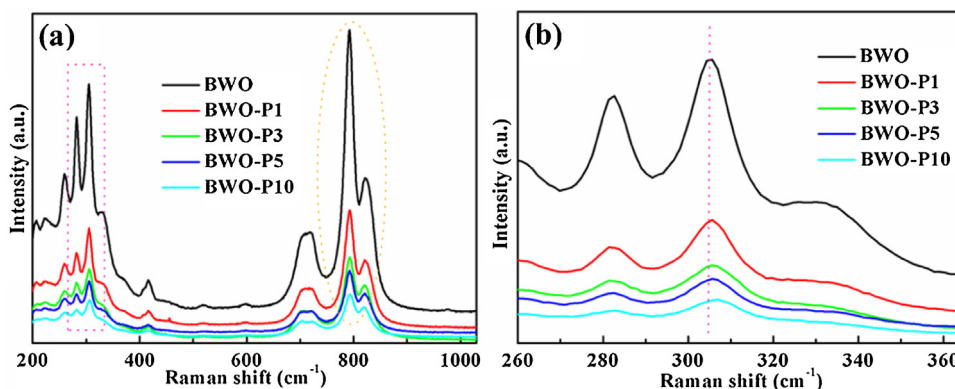


Fig. 2. Raman spectra of BWO, BWO-P1, BWO-P3, BWO-P5 and BWO-P10 (a), magnified peaks located at from 260 cm^{-1} to 360 cm^{-1} (b).

The internal microstructural characteristic and the PO_4 doping state in the samples are further investigated by TEM technique. Fig. 3a–c further shows that BWO-P5 sample exhibits the micro-spherical architecture feature constructed by nanosheets. The interplanar spacing of the nanosheet observed from HRTEM is 0.193 nm (Fig. 3d), which agrees well with the (220) planes of orthorhombic Bi_2WO_6 identically. The corresponding SAED pattern in Fig. 3e shows a clear square diffraction spot array, indicating this sample has high crystallinity. The labeled diffraction spots correspond to (200) and (020) lattice planes owing to their interplanar spacing of 0.273 nm and 0.272 nm, respectively. To further investigate the PO_4 doping state and the spatial uniformity of the elemental distribution accurately, HR-TEM EDS elemental mapping is carried out on a single microsphere. Fig. 3c shows a high-angle annular dark-field (HAADF) image of a single BWO-P5 particle. The EDS elemental maps in Fig. 3f–i demonstrates that Bi, W, O and P elements distribute homogeneously throughout the microsphere, and there is no other obvious compositional distribution among the whole architecture. These results further prove that the PO_4 has been doped into the Bi_2WO_6 lattice uniformly without producing any impurities, which are in line with the analyses of XRD and Raman scattering spectra.

3.3. Chemical composition and surface states of as-prepared samples

To obtain more information about the dopant chemical composition and surface states, XPS analysis are conducted on BWO and BWO-P5 samples. As observed in Fig. S3, the survey XPS spectra show the obvious binding energy peaks attribute to W 4f, Bi 4f, W 4d, Bi 4d, O 1s, Bi 4p, P 2p state and O auger state, respectively. Furthermore, the broad signal peak of P 2p state at about 132.9 eV is obviously observed from the high-resolution XPS spectrum of BWO-P5 (Fig. 4a), further confirming the existence of P^{5+} [32], which is also in accordance with the EDS analysis in Fig. S4. In addition, the XPS spectra of Bi in BWO sample (Fig. 4b) can be assigned to the binding energies of Bi^{3+} 4f_{7/2} and 4f_{5/2} states at 158.9 eV and 164.3 eV, respectively [33]. The obvious binding energy peaks at 35.2 eV and 37.4 eV of W in BWO sample derive from W^{6+} 4f_{7/2} and 4f_{5/2} states (Fig. 4c) [34]. It is noted that the binding energies of Bi 4f state and W 4f state in BWO-P5 sample shift 0.3 eV and 0.4 eV toward high binding energy compared with that of BWO, respectively, which should be closely related to PO_4 doped in the sample. It was reported that the electron concentration decrease can reduce the electron screening effect, resulting in strengthening the binding energy [35,36]. PO_4 doped can decrease the surrounding electron concentration of Bi^{3+} and W^{6+} because P has higher electronegativity compared to W, thus leading to the shift to the higher binding energy of Bi and W elements in XPS

spectra as expected. Meanwhile, the introduction of PO_4 into the lattice matrix of Bi_2WO_6 may form crystal defect (oxygen vacancy) because it replaces WO_4 with W^{6+} oxidation state. Fig. 4d shows the XPS spectra of O 1s state for BWO and BWO-P5 samples, where the peak at 531.8 eV of BWO-P5 sample is related to the oxygen vacancies on the surface [37]. The peak at 529.5 eV is assigned to the crystal lattice oxygen [37]. To further confirm the formation of oxygen vacancy, the EPR technique is further carried out. As can be seen from Fig. S5, the BWO-P5 sample gives rise to a stronger signal peak at $g \approx 2.001$ compared with BWO, which is regarded as the surface oxygen vacancy feature [38]. The presence of surface oxygen vacancy can facilitate charge transfer and reduce hole-electron recombination, thus improving photocatalytic activity [39].

3.4. Photocatalytic degradation activity over as-prepared photocatalysts

It is widely known that Cr(VI) contamination in natural water has harmful effects on human health. Green photocatalysis technology is recognized as a promising way for reducing Cr(VI) to the less toxic Cr(III) due to its unique advantage [40,41]. So we first investigate the photocatalytic activity of as-prepared samples through reduction of Cr(VI). As can be observed from Fig. 5a, all the PO_4 doped Bi_2WO_6 samples show the higher reducing Cr(VI) activity compared with the pristine Bi_2WO_6 . In particular, the BWO-P5 sample shows the highest reducing Cr(VI) activity, which removes completely Cr(VI) only within 40 min. The photocatalytic activity enhancement may be due to the doped PO_4 increasing the separation of photoinduced electron-hole pairs and specific surface areas as described above. However, excessive dopants may act as recombination centers of charge carriers, which is bad for enhancing photocatalytic activity [22]. Furthermore, the removal rate constant k of Cr(VI) reduction is estimated through the plots of $\ln(C_0/C)$ vs irradiation time, because the kinetic curve of Cr(VI) reduction approximates as a pseudo-first-order process [42]. The plots of $\ln(C_0/C)$ vs irradiation time and the corresponding removal rate constant k values for all the samples are provided in Fig. S6. The k values over BWO-P5 sample is 0.159 min^{-1} , which reaches to 19.15, 8.37, 5.89 and 2.65 times as much as that of BWO (0.0083 min^{-1}), BWO-P1 (0.019 min^{-1}), BWO-P3 (0.027 min^{-1}) and BWO-P10 (0.06 min^{-1}), respectively. In addition, it is well known that the photocatalytic activity is closely related to the separation efficiency of photogenerated electron-hole pairs. Therefore, citric acid serving as the sacrificial agent is introduced into the reaction system to improve the separation efficiency of electron-hole pairs, because it can capture photogenerated holes due to its electron rich property. The controlled experiments of photocatalytic reduction Cr(VI) solution over BWO-P5 sample under visible light are performed. As shown in Fig. 5b, the fast and complete reduction of Cr(VI) is

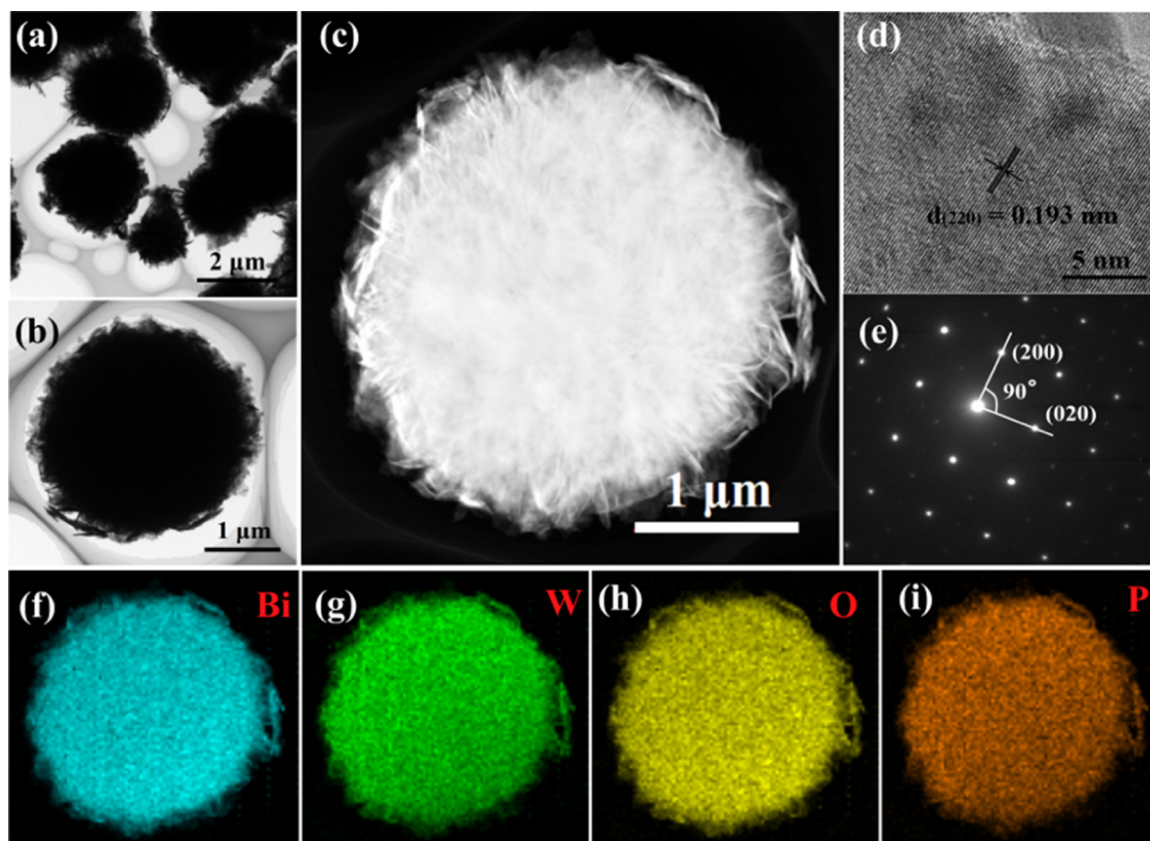


Fig. 3. TEM images of BWO-P5 sample (a, b), HRTEM image of the nanosheet units and the corresponding SAED pattern (e), HAADF image of an individual microsphere of BWO-P5 sample (c) and the corresponding XEDS energy mapping of Bi (f), W (g), O (h) and P (i).

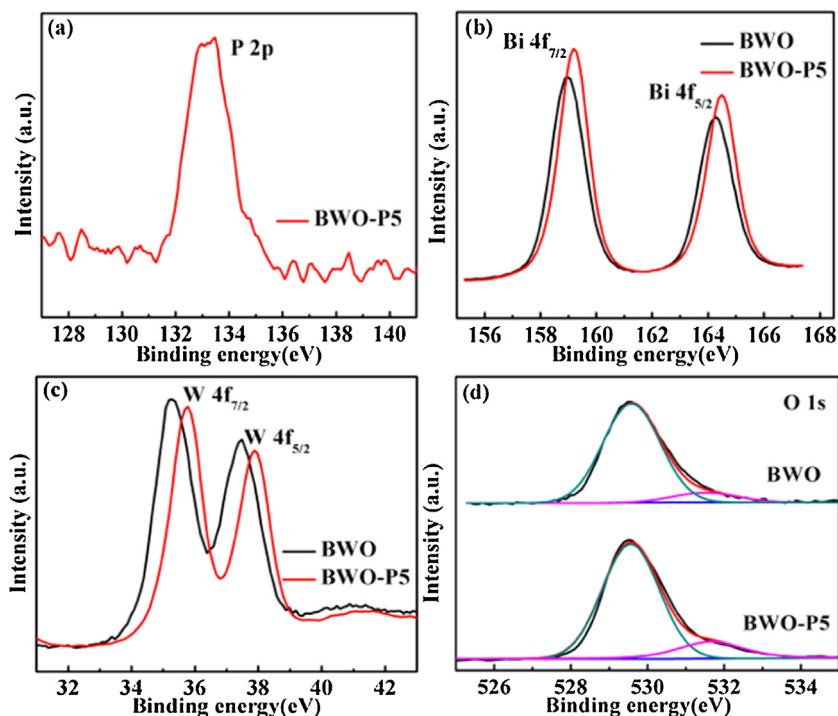


Fig. 4. High-resolution XPS spectra of P 2p (a) for BWO-P5 sample, Bi 4f (b), W 4f (c) and O 1s (d) spectrum for BWO and BWO-P5 samples.

realized over the BWO-P5 sample in the presence of citric acid in the reaction system. However, when there is citric acid alone, only a small part of Cr(VI) is reduced. It may be due to that the elec-

trons in the hydroxyl group in the citric acid carboxyl are excited under the light irradiation to move into the empty d orbitals of Cr(VI), leading to the reduction of Cr(VI) [42]. Simultaneously, in

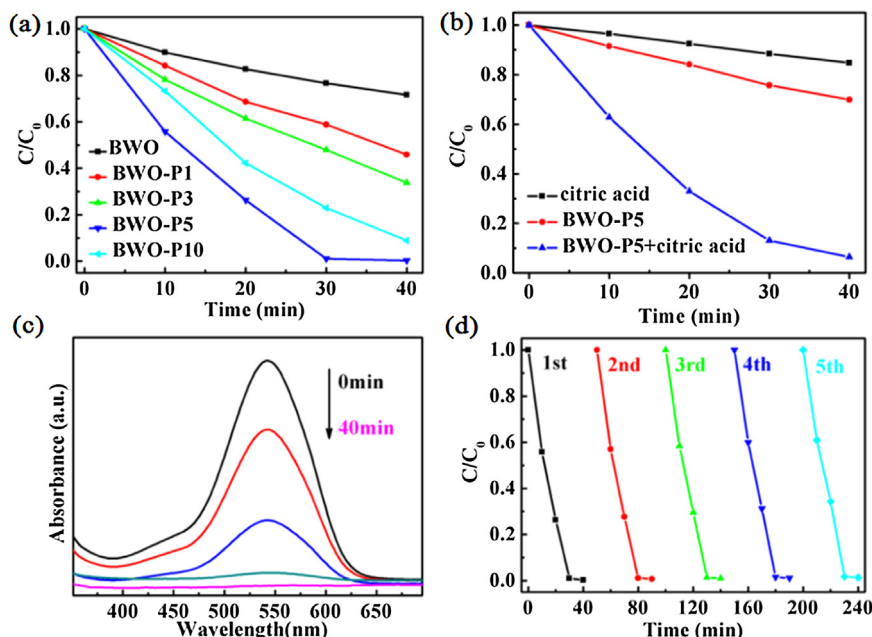


Fig. 5. Dynamic curves of Cr(VI) photoreduction over different samples (a), photoreduction of Cr(VI) solutions under different conditions (b), absorption spectra variations (c) and cycle runs (d) of Cr(VI) solutions over BWO-P5 sample.

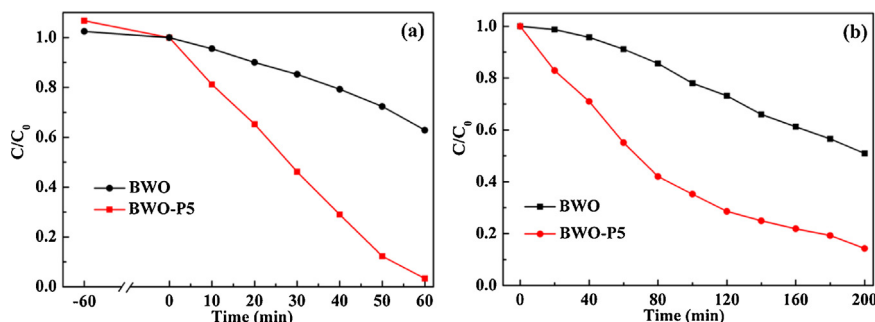


Fig. 6. Dynamic curves of photodegradation RhB solution (a) and phenol solution (b) over BWO and BWO-P5 samples.

the absence of citric acid, BWO-P5 sample also shows much lower photocatalytic activity than that in the presence of citric acid. Obviously, the synergistic effect between citric acid and BWO-P5 plays a crucial role for improving the photoreduction of Cr(VI). Additionally, the absorbance variation of Cr(VI) solutions during the reduction process over the BWO-P5 sample are described in Fig. 5c. It is notable that the absorbance of Cr(VI) solution completely disappears after 40 min, which demonstrates the Cr(VI) are reduced entirely to Cr(III). Meanwhile, the reusability and stability of the photocatalysts are also crucial factors for practical application. As can be seen from Fig. 5d, the reducing Cr(VI) activity of BWO-P5 shows hardly any loss after five cycles reuse, which confirms that BWO-P5 is a stable photocatalyst during the photocatalytic reducing Cr(VI) solution.

Besides Cr(VI) solution, the colored dyes and colorless phenols are common industrial organic pollutants [43]. In the work, the typical RhB dye and phenol are further selected as representatives to discuss the photocatalytic activity of the as-prepared samples. Fig. 6a shows the degradation dynamic curves of the colored RhB dye, BWO-P5 presents the much splendid photocatalytic degradation ability than that of BWO and it completely decomposes RhB dye molecules within 60 min. Meanwhile, BWO-P5 presents the stronger adsorption capacity compared with that of BWO (Fig. 6a). Because the superior adsorption capacity contributes to improv-

ing photocatalytic activity owing to the full contact between target molecules and photocatalyst [44], it is another reason for improved photocatalytic activity over BWO-P5 sample. In addition, the kinetic characteristic of RhB degradation is also investigated by fitting its kinetic curve according to an approximated pseudo-first-order process [45]. Fig. S7 shows the plots of $\ln(C_0/C)$ versus irradiation time and the fitting results of these plots. The calculated removal rate constant k of RhB dye over BWO-P5 is 0.0529 min^{-1} , which reaches to 7.15 times attractively as much as that of BWO (0.014 min^{-1}). Meanwhile, the cycle runs of BWO-P5 are carried out owing to its importance in practical application. Fig. S8 exhibits clearly that the photocatalytic activity of BWO-P5 is barely reduction after reusing five recycles. Besides, the degradation dynamic curves of colourless phenol solution over BWO and BWO-P5 samples in Fig. 6b shows that the phenol solution is decomposed more than 90% after 200 min over the BWO-P5 sample under visible light irradiation, which is much higher than that of BWO (only lower 50%). The above results demonstrate that the PO_4 -doped Bi_2WO_6 sample enhance distinctly the colored dyes and colourless phenols photocatalytic degradation ability.

Moreover, antibiotics are one kind of the most common pharmaceuticals found in the aquatic environment, which are recognized as one of the serious emerging issues in environmental chemistry because their antimicrobial nature prevents effective removal in

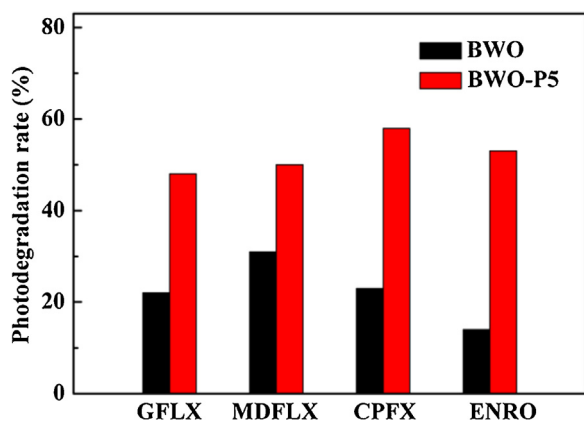


Fig. 7. Photodegradation rates of various antibiotics over BWO and BWO-P5 samples.

sewage treatment process [46,47]. Therefore, for the sake of investigating the universal enhanced photocatalytic activity of PO_4 -doped Bi_2WO_6 sample, the photodegradation experiments for the four kind common antibiotics over the as-prepared samples under visible light are carried out, including gatifloxacin (GFLX), danofloxacin mesylate (DFLXM), ciprofloxacin (CPFX), enrofloxacin hydrochloride (ENRO). As shown in Fig. 7, the degradation rates of these four kind common antibiotics over BWO-P5 sample are all greater than that over BWO sample at the same reaction time of 140 min. The degradation rate of GFLX, DFLXM, CPFX and ENRO over BWO-P5 sample is 2.18, 1.61, 2.52 and 3.79 times higher as much as that over BWO sample, respectively. All above results prove that the PO_4 -doped Bi_2WO_6 sample enhance photocatalytic activity universally, which may become the promising photocatalyst for practical application due to its universality for decomposing the various contaminants in water.

3.5. Possible photocatalytic reaction mechanisms for organic pollutants over BWO-P5 sample

Based on the above analysis, taking RhB dye and CPFX as examples, the possible photocatalytic degradation mechanisms for organic pollutants over BWO-P5 sample are proposed as follows: when the BWO-P5 sample is exposed to the visible light, the electrons can be excited firstly from VB to CB for forming photogenerated electron-hole pairs on the sample surface. Then the electrons and holes separate and transfer to the corresponding conduction band and valence band, respectively. As a result, the photocatalytic reactions of organic pollutants molecules degradation can be taken place on the surface of BWO-P5 sample. As can be seen from Fig. S9a, for the RhB dye photodegradation under visible light, when the TEOA is added into photocatalytic reaction system, the photodegradation rate is only 0.6%. It implies that hole (h^+) has intensively effect on the RhB photodegradation. However, when the DMSO and BQ are added into reaction solution, the degradation rate of RhB dye is almost unanimous, which is 48% and 49%, respectively. It indicates that hydroxyl radicals ($\cdot\text{OH}$) and superoxide radical ($\cdot\text{O}_2^-$) are also the main activated species. Thus, the influence order of the activated species in the process photodegradation for RhB dye is $h^+ > \cdot\text{O}_2^- = \cdot\text{OH}$. In the same way, as can be seen from Fig. S9b of the CPFX photodegradation under visible light, the photodegradation rate of CPFX still reaches to $\sim 45.5\%$ in the presence of IPA, which is slightly lower than that of no scavenger existence ($\sim 58.2\%$) at the same time. But when the TEOA and BQ are presence in reaction system, the CPFX photodegradation rates are declined significantly, which is only $\sim 7.2\%$ and $\sim 27.7\%$, respectively. It indicates that h^+ and $\cdot\text{O}_2^-$ are the main activated species. The influence order of the

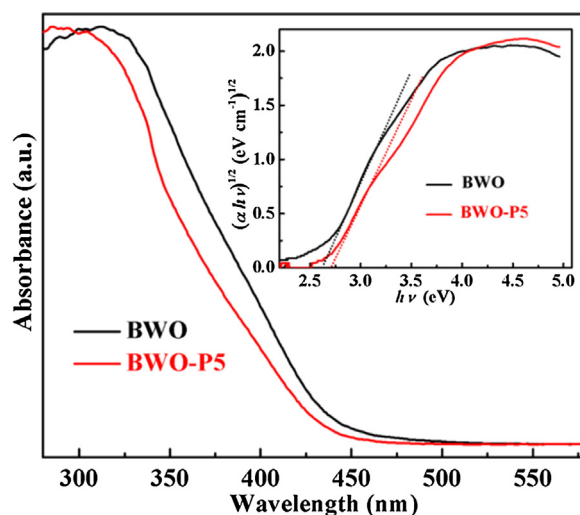


Fig. 8. UV-vis DRS and plots of $(\alpha h\nu)^{1/2}$ versus $h\nu$ (the insert) of BWO and BWO-P5 samples.

photodegradation process for CPFX is $h^+ > \cdot\text{O}_2^- > \cdot\text{OH}$. In addition, in order to further explore the photodegradation reaction mechanism of organic pollutants over BWO-P5 sample, the ESR technique is carried out to detect the active species during the photodegradation process over BWO-P5 sample under visible light. As seen in Fig. S10a, four characteristic peaks of $\text{DMPO} \cdot \cdot\text{O}_2^-$ species are observed in methanol dispersion of BWO-P5 sample under visible light irradiation. Meanwhile, the characteristic peaks of $\text{DMPO} \cdot \cdot\text{OH}$ species are also detected in BWO-P5 aqueous dispersions under visible light irradiation (Fig. S10b). Therefore, the radicals trap experiments and ESR results demonstrate that $\cdot\text{O}_2^-$, $\cdot\text{OH}$ and photogenerated holes are the main active species during the photocatalytic process.

3.6. Light absorption, valence band spectra and flat-band potential measurement of the BWO and BWO-P5 samples

In order to obtain an insight into reasons of improving photocatalytic activity of PO_4 -doped Bi_2WO_6 sample, the light absorption, valence band spectra, luminescent decay, photoluminescence spectra and photoelectricity etc. physical properties that significantly influence photocatalytic activity are investigated in detail. The UV-vis DRS spectra of BWO and BWO-P5 samples are measured to evaluate light absorption property. From Fig. 8, both of the UV-vis DRS spectra shapes are almost same and exhibit the obviously visible harvest ability. Meanwhile, the clear knee point in BWO-P5 sample from Fig. 8 suggests the impurity level can be generated after doping PO_4 . In addition, the absorption edge of BWO-P5 sample is blue shift compared with that of BWO sample obviously. The specific band gap values of as-prepared samples are further estimated according to the research method of crystal semiconductor reported by M. A. Butler (See Supporting information) [48]. Because Bi_2WO_6 is a typical indirect band gap semiconductor [9], we achieve the light band gap values of BWO (2.62 eV) and BWO-P5 (2.71 eV) using the plots of $(\alpha h\nu)^{1/2}$ versus $h\nu$, respectively (the insert of Fig. 8).

For the sake of corroborating the band structure variation, the values of the relative conduction band (CB) and valence band (VB) position for BWO and BWO-P5 samples are calculated in Table S1. The CB and VB values of BWO-P5 sample shift up ~ 0.04 eV and move down ~ 0.05 eV in comparison with that of BWO sample, respectively. Furthermore, the VB variation of BWO-P5 sample is verified by the investigation of XPS VB spectra. It is found from Fig. 9a that the VB potential of BWO-P5 sample moves down $0-0.04$ eV compared with that of BWO, which is almost unanimous with the

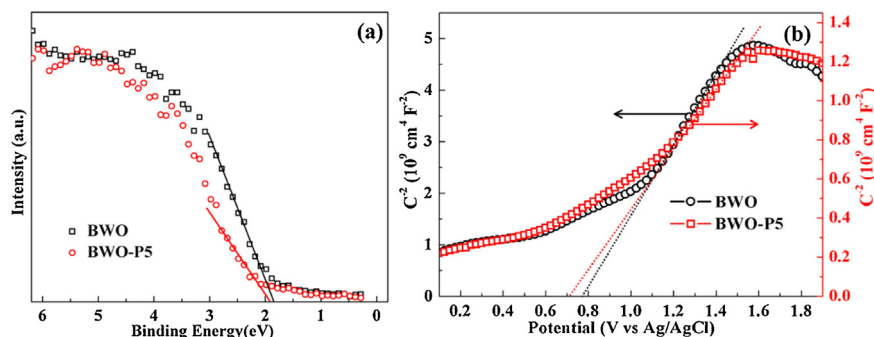


Fig. 9. XPS valence band spectra (a) and Mott-Schottky plots (b) of BWO and BWO-P5 samples.

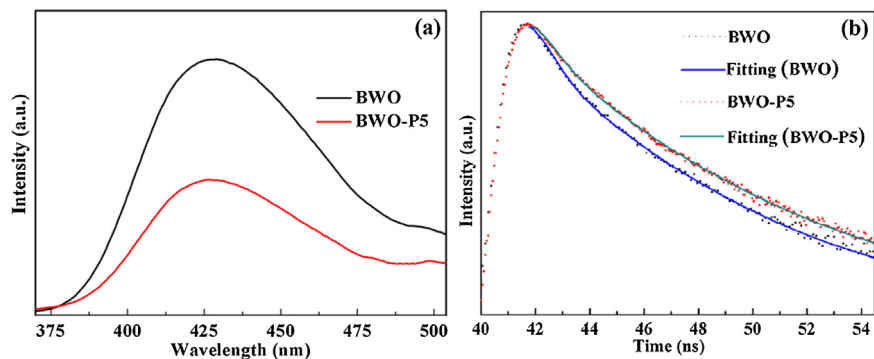


Fig. 10. PL spectra (a) and fluorescence decay curves (b) of BWO and BWO-P5 samples.

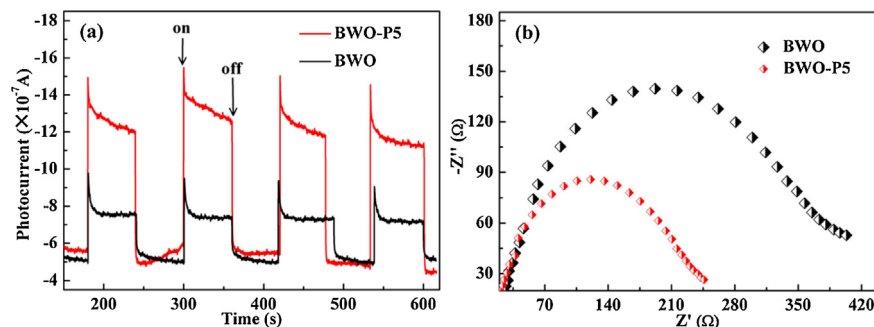


Fig. 11. Photocurrent response (a) and EIS spectra (b) of BWO and BWO-P5 samples.

calculated value. Moreover, the CB variation of BWO-P5 sample is investigated by using flat-band potential measurement. Fig. 9b shows the Mott-Schottky plots of the BWO and BWO-P5 film as an electrode, respectively, the positive slope of which in the linear region indicates they are in line with the feature of n-type semiconductor [49]. It is also found that the flat-band potential position of BWO-P5 (0.72 V) is lower 0.04 V than that of BWO (0.76 V) under the same experimental conditions, which is also agreed with the calculated value. As mentioned above, we can further deduce that the more negative CB position and more positive VB position of BWO-P5 compared with that of BWO can result in improving photocatalytic activity due to the effects of high redox ability.

3.7. Photoluminescence spectra, luminescent decay and photoelectrochemical properties of BWO and BWO-P5 samples

The effective generation and separation of photogenerated charge carriers are prerequisite for photocatalytic reactions, it is reported the intensity of PL emission spectroscopy reflects indirectly the recombination degree of charge carriers [50,51]. As

shown in Fig. 10a, relative to BWO, the PL peak intensity of BWO-P5 at ~425 nm reduces obviously, indicating that the recombination of electron-hole pairs is largely impeded after doping PO_4 . Moreover, the recombination of electron-hole pairs is also characterized by the lifetime of carriers. A longer fluorescent lifetime implies lower charge carrier recombination rate, and thus higher photocatalytic activity [52]. The fluorescence decay curves of BWO and BWO-P5 are shown in Fig. 10b. Through fitting the decay spectra, we can obtain that the lifetime of BWO-P5 (19.6 ns) is longer than that of BWO (16.3 ns). The result demonstrates that doped PO_4 contributes to the photocatalytic activity in a way that increased the possibility of charge carrier which takes part in the photocatalytic reactions.

In addition, the higher separation efficiency of electron-hole pairs over BWO-P5 sample is further confirmed by the photocurrent measurement which is able to investigate qualitatively the separation efficiency of photon-generated charge carriers in the photocatalytic reactions [53,54]. It can be obviously seen from Fig. 11a that rapid and stable photocurrent responses are detected in both BWO and BWO-P5 as electrodes under visible light illumination, respectively. Importantly, the photocurrent response for

BWO-P5 is much higher than that of BWO, which reveals that the doping PO₄ efficaciously elevates the interfacial charge separation and transfer. In addition, electrochemical impedance spectroscopy (EIS) is another valid electrochemical strategy to account for the electron-transfer efficiency on the electrodes [55]. In general, a higher mobility and separation of photoexcited electron-hole pairs will result in a smaller EIS arc radius. From Fig. 11b, BWO-P5 features significantly smaller radius than that of BWO, demonstrating that a fast interfacial charge transfer property in the BWO-P5 sample. All above results indicate PO₄ doping has a positive action on the separation and transfer of photogenerated charge carriers, which is in accordance with the apparently improved photocatalytic activity of BWO-P5 sample.

4. Conclusions

In conclusion, a highly efficient PO₄-doped Bi₂WO₆ photocatalyst is prepared firstly via the urea-precipitation method in the hydrothermal process. The PO₄-doped Bi₂WO₆ sample shows the higher photocatalytic activity than that of pristine Bi₂WO₆ for the degradation of Cr(VI), RhB dye, phenol and antibiotics etc. various pollutants under visible light irradiation. One reason of enhanced photocatalytic degradation activity is that PO₄ doping lifts up and moves down CB position and VB position of Bi₂WO₆ sample, respectively, thus increasing the redox ability. Moreover, PO₄-doped Bi₂WO₆ sample facilitates the separation of photo-generated charge carriers, which is another reason for improving photocatalytic activity. The present work not only provides the feasibility of anionic group acting as an efficient dopant to improve the photocatalytic activity for environmental purification, but also gives a new direction to design other high-efficiency semiconductor photocatalyst for practical applications.

Acknowledgment

This work was financially supported by projects of Natural Science Foundation of China (21501035, 21271055 and 21471040), the Fundamental Research Funds for the Central Universities (HIT-IBRSEM. A. 201410) and China Postdoctoral Science Foundation funded project (2015M570298). We acknowledge the support provided by Open Project of State Key Laboratory of Urban Water Resource and Environment, Harbin Institute of Technology (No. QAK201304), Program for Innovation Research of Science in Harbin Institute of Technology (PIRS of HIT B201412 and B201508).

Appendix A. Supplementary data

Supplementary data associated with this article can be found, in the online version, at <http://dx.doi.org/10.1016/j.apcatb.2016.01.054>.

References

- [1] A. Kudo, Y. Miseki, *Chem. Soc. Rev.* 38 (2009) 253–278.
- [2] H.J. Dong, G. Chen, J.X. Sun, C.M. Li, Y.G. Yu, D.H. Chen, *Appl. Catal. B: Environ.* 134–135 (2013) 46–54.
- [3] X.L. Yu, A. Shavel, X.Q. An, Z.S. Luo, M. Ibáñez, A. Cabot, *J. Am. Chem. Soc.* 136 (2014) 9236–9239.
- [4] K.Y. Song, M.K. Park, Y.T. Kwon, H.W. Lee, W.J. Chung, W.I. Lee, *Chem. Mater.* 13 (2001) 2349–2355.
- [5] X.B. Chen, L. Liu, F.Q. Huang, *Chem. Soc. Rev.* 44 (2015) 2019.
- [6] T. Leshuk, R. Parviz, P. Everett, H. Krishnakumar, R.A. Varin, F. Gu, *ACS Appl. Mater. Interfaces* 5 (2013) 1892–1895.
- [7] S.W. Verbruggen, M. Keulemans, M. Filippousi, D. Flahaut, G. Van Tendeloo, S. Lacombe, J.A. Martens, S. Lenaerts, *Appl. Catal. B: Environ.* 156–157 (2014) 116–121.
- [8] Y. Houman, L. Zhi, C. Yao, T.N. Huong, R.B. Venkat, J. Babu, S.Q. Ma, S. Rudy, T.T. Arash, *ACS Catal.* 5 (2015) 327–335.
- [9] C.M. Li, G. Chen, J.X. Sun, H.J. Dong, Y. Wang, C.D. Lv, *Appl. Catal. B: Environ.* 160–161 (2014) 383–389.
- [10] L.S. Zhang, W.Z. Wang, L. Zhou, H.L. Xu, *Small* 3 (2007) 1618–1625.
- [11] N. Zhang, R. Ciriminna, M. Pagliaro, Y.Y. Xu, *Chem. Soc. Rev.* 43 (2014) 5276–5287.
- [12] L.S. Zhang, H.L. Wang, Z.G. Chen, P.K. Wong, J.S. Liu, *Appl. Catal. B: Environ.* 106 (2011) 1–13.
- [13] L.W. Zhang, Y. Man, Y.F. Zhu, *ACS Catal.* 1 (2011) 841–848.
- [14] Y. Fu, C. Chang, P. Chen, X.L. Chu, L.Y. Zhu, *J. Hazard. Mater.* 254 (2013) 185–192.
- [15] R. Shi, G.L. Huang, J. Lin, Y.F. Zhu, *J. Phys. Chem. C* 113 (2009) 19633–19638.
- [16] Y.F. Yang, Y.G. Li, L.P. Zhu, H.P. He, L. Hu, J.Y. Huang, F.C. Hu, B. He, Z.Z. Ye, *Nanoscale* 5 (2013) 10461–10471.
- [17] S. Tonda, S. Kumar, S. Kandula, V. Shanker, *J. Mater. Chem. A* 2 (2014) 6772–6780.
- [18] Z.J. Zhang, W.Z. Wang, W.Z. Yin, M. Shang, L. Wang, S.M. Sun, *Appl. Catal. B: Environ.* 101 (2010) 68–73.
- [19] H.B. Fu, S.C. Zhang, T.G. Xu, Y.F. Zhu, J.M. Chen, *Environ. Sci. Technol.* 42 (2008) 2085–2091.
- [20] X. Ding, K. Zhao, L.Z. Zhang, *Environ. Sci. Technol.* 48 (2014) 5823–5831.
- [21] W.J. Jo, J.W. Jang, K.J. Kong, H.J. Kang, J.Y. Kim, H.C. Jun, K.P.S. Parmar, J.S. Lee, *Angew. Chem. Int. Ed.* 51 (2012) 3147–3151.
- [22] H.W. Huang, X.W. Li, J.J. Wang, F. Dong, P.K. Chu, T.R. Zhang, Y.H. Zhang, *ACS Catal.* 5 (2015) 4094–4103.
- [23] S. Kohtani, S. Makino, A. Kudo, K. Tokumura, Y. Ishigaki, T. Matsunaga, O. Nikaido, K. Hayakawa, R. Nakagaki, *Chem. Lett.* 31 (2002) 660–661.
- [24] J. Liu, G.L. Liu, M.Z. Li, W.Z. Shen, Z.Y. Liu, J.X. Wang, J.C. Zhao, L. Jiang, Y.L. Song, *Energy Environ. Sci.* 3 (2010) 1503–1506.
- [25] J.S. Wang, Y.L. Yu, S. Li, L.M. Guo, E.J. Wang, Y.A. Cao, *J. Phys. Chem. C* 117 (2013) 27120–27126.
- [26] X.Y. Xiao, J. Nogan, T. Beechem, G.A. Montaño, C.M. Washburn, J. Wang, S.M. Brozik, D.R. Wheeler, D.B. Burckel, R. Polsky, *Chem. Commun.* 47 (2011) 9858–9860.
- [27] M. Mączka, A.F. Fuentes, L. Kępiński, M.R. Diaz-Guillen, J. Hanuza, *Mater. Chem. Phys.* 2–3 (2010) 289–295.
- [28] M. Mączka, L. Macalik, K. Hermanowicz, L.K. Pinski, P. Tomaszewski, *J. Raman Spectrosc.* 41 (2010) 1059–1066.
- [29] M. Crane, R.L. Frost, P.A. Williams, J.T. Klopogge, *J. Raman Spectrosc.* 33 (2002) 62–66.
- [30] Y.Y. Li, J.P. Liu, X.T. Huang, J.G. Yu, *Dalton Trans.* 39 (2010) 3420–3425.
- [31] L.S. Zhang, W.Z. Wang, Z.G. Chen, L. Zhou, H.L. Xu, W. Zhu, *J. Mater. Chem.* 17 (2007) 2526–2532.
- [32] C.S. Pan, J. Xu, Y.J. Wang, D. Li, Y.F. Zhu, *Adv. Funct. Mater.* 22 (2012) 1518–1524.
- [33] D.J. Wang, G.L. Xue, Y.Z. Zhen, F. Fu, D.S. Li, *J. Mater. Chem.* 22 (2012) 4751–4758.
- [34] J.H. Ryu, S.Y. Bang, W.S. Kim, G.S. Park, K.M. Kim, J.W. Yoon, K.B. Shim, N. Koshizaki, *J. Alloys Compd.* 441 (2007) 146–151.
- [35] X.H. Li, H.Y. Xu, X.T. Zhang, Y.C. Liu, J.W. Sun, Y.M. Lu, *Appl. Phys. Lett.* 95 (2009) 1919031–1919033.
- [36] Z.Y. Zhang, C.L. Shao, X.H. Li, Y.Y. Sun, M.Y. Zhang, J.B. Mu, P. Zhang, Z.C. Guo, Y.C. Liu, *Nanoscale* 5 (2013) 606–618.
- [37] E. Silva Junior, F.A. La Porta, M.S. Liu, J. Andrés, J.A. Varela, E. Longo Lin, *Dalton Trans.* 44 (2015) 3159–3175.
- [38] F.T. Li, Q. Wang, J.R. Ran, Y.J. Hao, X.J. Wang, D.S. Zhao, S.Z. Qiao, *Nanoscale* 7 (2015) 1116–1126.
- [39] Y.H. Lv, Y.F. Liu, Y.Y. Zhu, Y.F. Zhu, *J. Mater. Chem. A* 2 (2014) 1174–1182.
- [40] Y. Yang, G.Z. Wang, Q. Deng, H.L. Ng Dickon, H.J. Zhao, *ACS Appl. Mater. Interfaces* 6 (2014) 3008–3015.
- [41] L.X. Yang, W.S. Sun, S.L. Luo, Y. Luo, *Appl. Catal. B: Environ.* 156–157 (2014) 25–34.
- [42] R.W. Liang, F.F. Jing, L.J. Shen, N. Qin, L. Wu, *J. Hazard. Mater.* (287) (2015) 364–372.
- [43] L.X. Yang, Y. Xiao, S.H. Liu, Y. Li, Q.Y. Cai, S.L. Luo, G.M. Zeng, *Appl. Catal. B: Environ.* 94 (2010) 142–149.
- [44] Z. Zhu, Z.Y. Lu, D.D. Wang, X. Tang, Y.S. Yan, W.D. Shi, Y.S. Wang, N.L. Gao, X. Yao, H.J. Dong, *Appl. Catal. B: Environ.* 182 (2016) 115–122.
- [45] C.M. Li, G. Chen, J.X. Sun, Y.J. Feng, H.J. Dong, Z.H. Han, Y.D. Hu, C.D. Lv, *New J. Chem.* 39 (2015) 4384–4390.
- [46] I.K. Konstantinou, T.A. Albanis, *Appl. Catal. B: Environ.* 49 (2004) 1–14.
- [47] J. Di, J.X. Xia, M.X. Ji, S. Yin, H.P. Li, H. Xu, Q. Zhang, H.M. Li, *J. Mater. Chem. A* 3 (2015) 15108–15118.
- [48] C.M. Li, G. Chen, J.X. Sun, Y.J. Feng, J.J. Liu, H.J. Dong, *Appl. Catal. B: Environ.* 163 (2015) 415–423.
- [49] M. Sun, G.D. Chen, Y.K. Zhang, Q. Wei, Z.M. Ma, B. Du, *Ind. Eng. Chem. Res.* 51 (2012) 2897–2903.
- [50] H.J. Dong, J.X. Sun, G. Chen, C.M. Li, Y.D. Hu, C.D. Lv, *Phys. Chem. Chem. Phys.* 16 (2014) 23915–23921.
- [51] J.Z. Ma, H.M. Wu, Y.C. Liu, H. He, J. Phys. Chem. C 118 (2014) 7434–7441.
- [52] P. Niu, L. Zhang, G. Liu, H.M. Cheng, *Adv. Funct. Mater.* 22 (2012) 4763–4770.
- [53] Z.H. Han, G. Chen, C.M. Li, Y.G. Yu, Y.S. Zhou, *J. Mater. Chem. A* 3 (2015) 1696–1702.
- [54] Y.H. Ng, I.V. Lightcap, K. Goodwin, M. Matsumura, P.V. Kamat, *J. Phys. Chem. Lett.* 1 (2010) 2222–2227.
- [55] H.J. Dong, G. Chen, J.X. Sun, Y.J. Feng, C.M. Li, C.D. Lv, *Chem. Commun.* 50 (2014) 6596–6599.